A NORMALIZATION METHOD FOR AXIAL-SHEAR STRAIN ELASTOGRAPHY

L. Chen, R. J. Housden, G. M. Treece,
A. H. Gee and R. W. Prager

CUED/F-INFENG/TR 645

9th April 2010

University of Cambridge
Department of Engineering
Trumpington Street
Cambridge CB2 1PZ
United Kingdom

Email: lc420/rjh80/gmt11/ahg/rwp @eng.cam.ac.uk

A normalization method for axial-shear strain elastography

Lujie Chen, R. James Housden, Graham M. Treece,
Andrew H. Gee and Richard W. Prager

University of Cambridge
Department of Engineering
Trumpington Street
Cambridge CB2 1PZ

Abstract

The axial-shear strain distribution of soft tissue contains information useful for differentiating benign and malignant tumours. This paper describes a novel axial-shear strain normalization method. The algorithm builds on an existing normalization procedure for axial strain in order to map the shear strain values to the range $[-\pi/2, \pi/2]$. The normalized shear data do not change sign with the direction of axial probe motion and therefore can be time averaged without loss of information. Experiments in simulation, *in vitro* and *in vivo* confirm the advantages of normalization. The proposed method is well suited to freehand strain imaging and enables the visualization of subtle slip patterns around inclusions.

1 Introduction

Ultrasonic elasticity imaging has been studied for more than fifteen years [1, 2]. Most of the research has focused on the axial strain of soft tissue under axial probe compression. The axial strain distribution has been used with some success in various clinical trials to differentiate benign and malignant tumours [3, 4, 5].

Recently, however, there has been interest in correlating the slip pattern of a suspicious inclusion to its malignancy [6]. There is some evidence to suggest that the slip pattern is better characterized by the axial-shear strain than the axial strain [7, 8, 9, 10, 11]. While the difference between the two is simply the direction of the gradient in the same axial displacement field, the two images have very different properties that impact on visualization[1].

Firstly, to the best of our knowledge, there is no prior work describing how to set the display range for a shear strain image. Most published shear strain images use a range related to the axial strain by a certain ratio, normally set by hand to obtain a subjectively pleasing image. This approach would be problematic for any clinically viable, real-time, freehand shear strain imaging system.

Secondly, unlike the axial strain where the absolute value is of interest, the shear strain is more useful when visualized as a signed quantity. This creates a problem when taking a time average that does not arise with axial strain [14]. If a sequence of shear strain fields is recorded with both compression and relaxation, the signed values from the different modes may cancel during time averaging, resulting in a loss of information.

Thirdly, the majority of data values in a shear strain field are close to zero, which makes it difficult to extract sufficient information to compensate for the variations in probe motion. Without compensation, visualization artefacts are often observed as rapidly changing background intensities in a time series.

All of the above issues suggest that a normalization method for shear strain imaging is desirable. A properly normalized shear strain field should allow automatic selection of the display range, preserve useful information in a signed, time-averaged image, and effectively compensate for the

[1]The axial-shear strain has a higher signal-to-noise ratio than the shear strain component obtained from the lateral displacements, the lateral-shear strain [7]. We therefore focus on axial-shear strain only. Although the proposed method may be useful for normalizing a combined axial- and lateral-shear strain field [12, 13], that is not the subject of this paper. Hereafter, we shall refer to axial-shear strain as shear strain, for simplicity.

variations in probe compression to arrive at a relatively stable visualization. In this paper, we propose a novel shear strain normalization method that builds on our existing work for axial strain [15], bringing the two tasks into a coherent framework. Simulation, *in vitro* and *in vivo* comparisons with an alternative visualization approach show that the proposed method produces superior time-averaged, shear strain images.

2 Method

An axial displacement field between two ultrasound radio-frequency (RF) frames can be calculated by any suitable algorithm: in this study, we used the hybrid algorithm described in [16]. The axial and shear strain data are obtained by taking the gradient of the displacement in the axial and the lateral directions respectively:

$$\varepsilon_{yy}(x,y) = \frac{\partial d_y(x,y)}{\partial y} \tag{1}$$

$$\varepsilon_{yx}(x,y) = \frac{\partial d_y(x,y)}{\partial x} \tag{2}$$

where y and x denote the axial and lateral directions respectively, d_y represents the axial displacement field, ε_{yy} is the axial strain and ε_{yx} is the shear strain.

The axial strain field can be normalized by fitting a two-dimensional (2D) function to the axial strain data. The function

$$s(x,y) = \alpha(1+\beta y)(1+\gamma x) \tag{3}$$

allows for typical stress variation in the axial and lateral directions [15]. The parameters α, β and γ are found by least-squares regression. Subsequently, the axial strain field is normalized by

$$\varepsilon'_{yy}(x,y) = \begin{cases} \varepsilon_{yy}(x,y)/s(x,y) & s(x,y) \neq 0 \\ 1 & s(x,y) = 0 \end{cases} \tag{4}$$

In the normalized axial strain field ε'_{yy}, 1 represents a pseudo-stiffness level equivalent to that of the background.

We propose that the same function s can also be used to normalize the shear strain field as follows:

$$\varepsilon'_{yx}(x,y) = \begin{cases} \arctan\left[\varepsilon_{yx}(x,y)/s(x,y)\right] & s(x,y) \neq 0 \\ 0 & s(x,y) = 0 \end{cases} \tag{5}$$

The normalized shear strain, ε'_{yx}, can be interpreted as the angle formed by the background axial strain and the shear strain, as shown in Figure 1. The advantages of this procedure are threefold. Firstly, all data are bounded within the range $[-\pi/2, \pi/2]$, so a display range can be selected with ease. Secondly, since s embodies an estimate of the axial and lateral stress variation, ε'_{yx} is compensated accordingly to produce a relatively uniform background. Thirdly, the sign of s is a reliable indicator of the probe's motion (compression or relaxation). Dividing ε_{yx} by s makes the sign of ε'_{yx} independent of this motion.

3 Experiments

The proposed normalization method was evaluated in simulation, *in vitro* and *in vivo*. A contrast measure was used to compare the quality of the normalized and the raw (unnormalized) shear strain images. The contrast measure generates one datum per shear strain field and is given by

$$C = \frac{\sum_{(x,y)\in U} \left| I_i(x,y) - \bar{I}_b \right|}{n\sigma_b} \tag{6}$$

where U represents a region of interest distinct from the background, n is the number of pixels (data points) in U, I_i is the pixel-wise displayed intensity (greyscale) in the region of interest, and

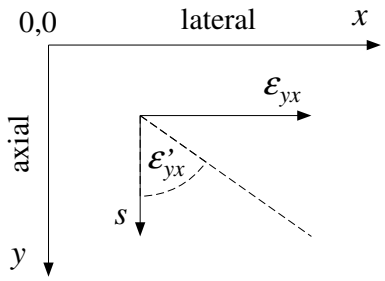

Figure 1: Formation of the normalized shear strain.

$\bar{I}_b$ and σ_b are the average and standard deviation respectively of the background intensity. The background is defined as any part of the image not in the region of interest. This metric is similar to the contrast-to-noise ratio [17] but does not include the standard deviation within the region of interest. This is because shear strain variation should not be considered as noise. Given a display range $[\varepsilon_{\min}, \varepsilon_{\max}]$, an intensity value (0–255) can be obtained from a shear strain datum according to

$$I = \begin{cases} 255 & \varepsilon \geq \varepsilon_{\max} \\ 0 & \varepsilon \leq \varepsilon_{\min} \\ (\varepsilon - \varepsilon_{\min})/(\varepsilon_{\max} - \varepsilon_{\min}) & \text{otherwise} \end{cases} \tag{7}$$

A fixed display range, $[-\pi/2, \pi/2]$, was used for the normalized shear strain, while a manually selected range was used for the raw shear strain, with specific values adjusted for each data set to give an image with subjectively optimal appearance. The contrast measure is relatively insensitive to the display range, as shown in Section 4.

3.1 Simulation

One probe compression and release cycle, comprising ten RF frames, was simulated. Figure 2 shows the three-dimensional (3D) probe motion at each frame with respect to an undeformed state. The motion was intended to mimic typical freehand scanning. At each frame, the 2D displacement field (axial and lateral) of a block of tissue with an elliptical, hard inclusion was calculated using finite element modelling (Abaqus 6.7, Simulia, Rhode Island, USA). The background and the inclusion had Young's moduli of 10 kPa and 40 kPa respectively. Both had a Poisson's ratio of 0.495. The major and minor axes of the inclusion measured 15 mm and 7.5 mm respectively. The boundary between the inclusion and the surrounding tissue was frictionless. Ultrasound RF signals were obtained by Field II [18]. The elevational displacement was introduced by offsetting the model in Field II. Noise was subsequently added at a signal-to-noise ratio of 30 dB. Field II simulation parameters were not untypical of clinical practice: a linear array probe of 128 elements, dynamic receive focusing, and a scanning region of $40 \times 40\,\text{mm}^2$.

3.2 Phantoms

Two phantom scans were recorded using a Diasus (Dynamic Imaging, Livingstone, UK) ultrasound machine with a 5–10 MHz linear array probe. The first scan captured a hard inclusion and the other a soft inclusion, both firmly bonded. They serve to illustrate the subtle differences between hard and soft inclusions' slip patterns.

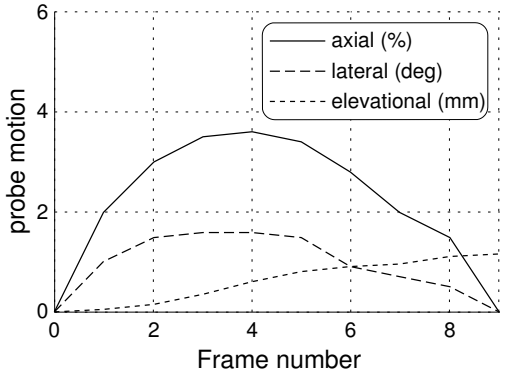

Figure 2: Simulated 3D motion of the probe with respect to an undeformed state. The axial motion is specified in terms of the average induced axial strain. The lateral motion involves an in-plane tilt around the centre of the transducer's scanning window. The elevational motion is a simple translation.

3.3 *In vivo* scan

An *in vivo* scan of a human brain was recorded using a Diasus ultrasound machine with a GE–RSP 6–12 MHz, mechanically swept, linear array probe[2]. The scan captured a brain tumour that was subsequently verified to be unbonded. The data was 2D: the reason for using a mechanically swept (3D) probe is that a larger contact area produces increased lateral stress [19], which helps to induce in-plane slip at material boundaries.

4 Results and Discussion

4.1 Simulation

The first, middle and last shear strain images of the simulated data set are shown in Figure 3. Each image was time averaged using all previously calculated frames: details of our time averaging procedure can be found in [15]. The display range applied to the raw shear strain data (d–f) was chosen to give a reasonable balance between the inclusion contrast and the background uniformity. All the shear strain images except (e) and (f) show good contrast between the interior of the inclusion and the background. Two factors contribute to this contrast: the frictionless boundary condition between the inclusion and the background [6], and the in-plane tilt of the probe (see Figure 2) which produces a "fill in" effect very similar to that observed with non-axially aligned, elliptical inclusions [20, 21]. Although the elliptical inclusion in this simulation was aligned axially, the tilt of the probe caused the inclusion to shift to the side, producing a similar shear strain pattern.

The benefits of normalization are subjectively clear. Normalized images do not vary significantly during a compression-release cycle, with relatively stable visual feedback. For a more objective assessment, we calculated the contrast coefficient (Equation 6) at each frame. The results are shown in Figure 4. For the raw shear strain images, we experimented with two display ranges. As can be seen, the resulting curves are almost coincident, indicating that the contrast metric is not sensitive to display range. The quality of the normalized shear strain images is markedly higher between frames 3 and 6. According to Figure 2, this is where the probe's axial displacement and tilt are small. Without normalization, the visibility of the slip pattern decreases

[2]Full ethical approval was obtained from the National Hospital for Neurology and Neurosurgery and the Institute of Neurology Joint Regional Ethics Committee (reference 08/H0716/92). Research and development approval and sponsorship was obtained from the Royal Free Hospital Clinical R&D Department (reference 7745).

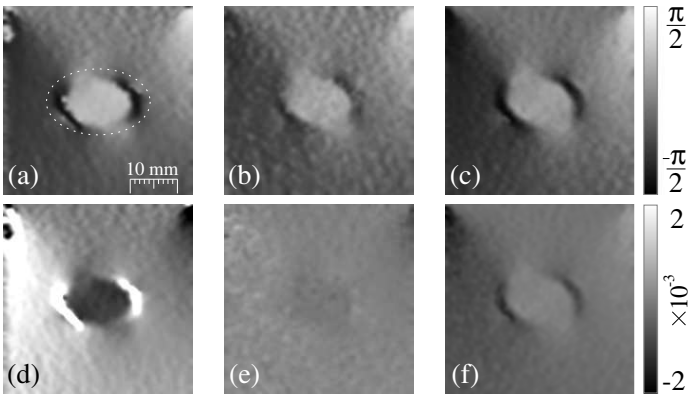

Figure 3: Results for the simulated data set. The (a) first, (b) middle and (c) last normalized shear strain fields. The (d) first, (e) middle and (f) last raw shear strain fields. Each image was time averaged using all previously calculated frames.

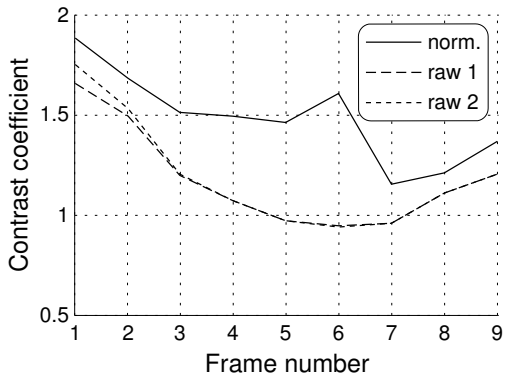

Figure 4: Contrast coefficients of the normalized and the raw shear strain images. The region of interest in Equation 6 encompassed the whole inclusion, as shown in Figure 3(a). Two display ranges, raw 1 $[-2\times10^{-3}, 2\times10^{-3}]$ and raw 2 $[-4\times10^{-3}, 4\times10^{-3}]$, were applied to the raw shear strain data.

significantly in such circumstances (Figure 3(e)).

4.2 Phantoms

Both of the phantom data sets comprise 50 shear strain fields. Typical B-mode and axial strain images are shown in Figures 6(a–b) and 7(a–b). Video results of the complete data sets accompany this paper, demonstrating a relatively stable shear strain image with normalization and a rapidly sign-switching output without. The contrast coefficients are shown in Figure 5. Apart from confirming the advantages of normalization, these results also suggest a difference in the two inclusions' degrees of bonding. The visibility, as reflected by the contrast, of the slip pattern around the soft inclusion is lower than that of the hard one, suggesting that it is more firmly bonded.

Given the stable output afforded by normalization, it is possible to differentiate the stiffness of an inclusion, as compared to the background, by examining the sign of the slip pattern. For example, Figures 6 and 7 show the 30th frame of each of the data sets. The raw strain images at frames 20 and 40 are also presented, to illustrate the instability without normalization. The dark slip quadrant of the hard inclusion in the normalized image (Figure 6(c), arrow), switches to

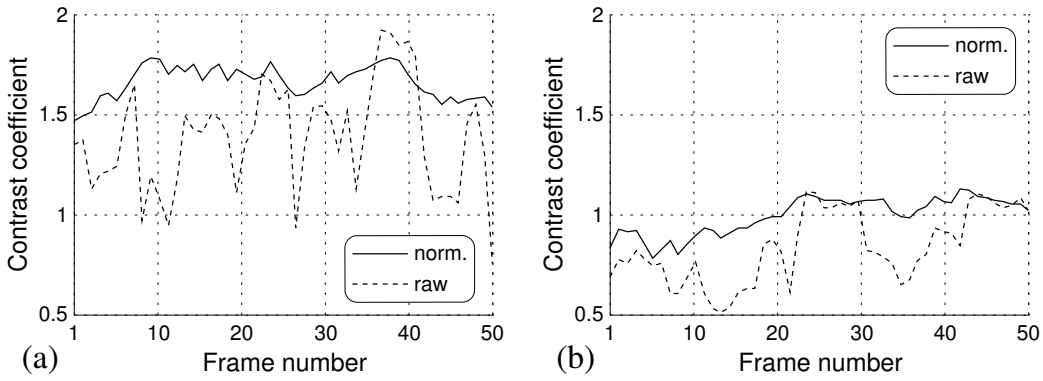

Figure 5: Contrast coefficients obtained from (a) the phantom with a hard inclusion and (b) the phantom with a soft inclusion. The coefficients were calculated under a progressive time average of ten frames. The regions of interest in Equation 6 were set to the annuli indicated in Figures 6(c) and 7(c).

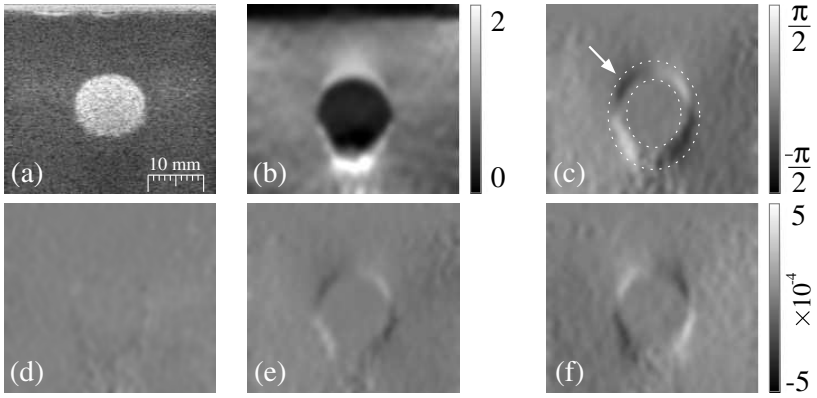

Figure 6: Results for the phantom with a hard inclusion. (a) B-mode image, (b) normalized axial strain and (c) normalized shear strain at frame 30. Raw shear strain at frames (d) 20, (e) 30 and (f) 40. The axial and shear strain images were obtained under a progressive time average of ten frames.

bright for the soft inclusion (Figure 7(c), arrow). One does not see such a determinable pattern in the raw images, because the sign of an unnormalized slip pattern is determined by both the inclusion's stiffness and the probe motion.

4.3 *In vivo* scan

The *in vivo* brain scan comprises 50 shear strain fields. The contrast coefficients, shown in Figure 8, demonstrate that the normalized approach outperforms the unnormalized one. A video of the complete sequence accompanies this paper. Figure 9 shows the 30th frame of the data set. The raw strain images at frames 20 and 40 are also presented. The axial strain image, Figure 9(b), suggests that the tumour is stiffer than the surrounding tissue: this was subsequently confirmed by histology. The raw shear strain images, Figures 9(d–f), indicate that there is a slip boundary around the tumour, but there is no clear contrast between the tumour and the background. Better contrast is evident in the normalized shear strain image, Figure 9(c). This is very likely the "fill in" effect [20, 21].

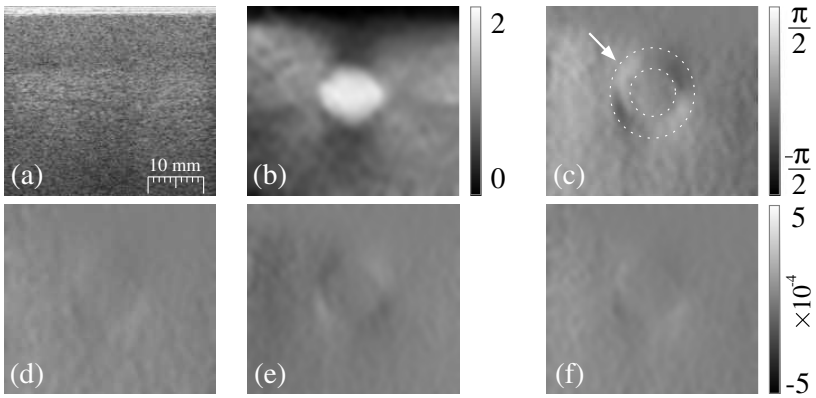

Figure 7: Results for the phantom with a soft inclusion. (a) B-mode image, (b) normalized axial strain and (c) normalized shear strain at frame 30. Raw shear strain at frames (d) 20, (e) 30 and (f) 40. The axial and shear strain images were obtained under a progressive time average of ten frames.

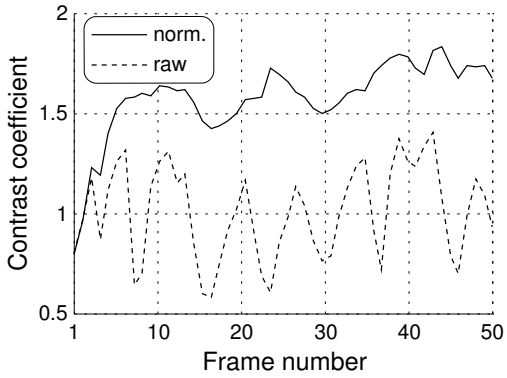

Figure 8: Contrast coefficients for the *in vivo* brain scan. The coefficients were calculated under a progressive time average of ten frames. The region of interest in Equation 6 was set to the tumour area indicated in Figure 9(a).

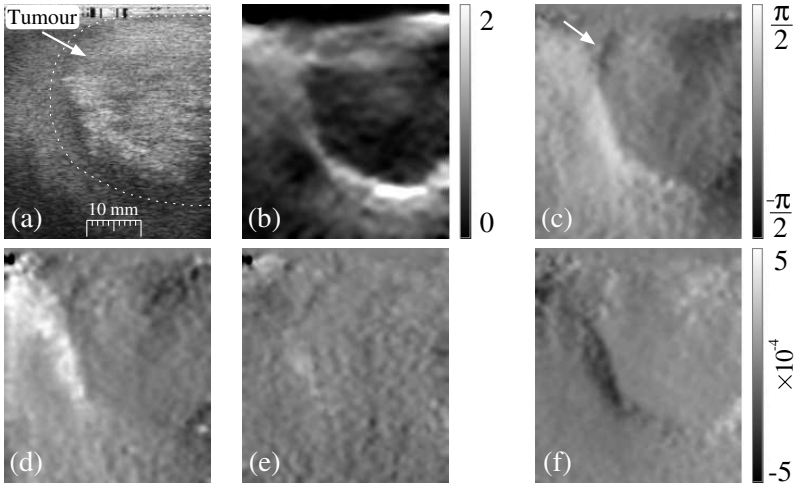

Figure 9: Results for the *in vivo* brain scan. (a) B-mode image, (b) normalized axial strain and (c) normalized shear strain at frame 30. Raw shear strain at frames (d) 20, (e) 30 and (f) 40. The axial and shear strain images were obtained under a progressive time average of ten frames.

In Figure 9(c), the arrow indicates a dark upper-left quadrant slip pattern, just like the one in Figure 6(c): this is further confirmation of the tumour's relative stiffness. The video shows that this pattern is stable in the normalized images, since it is determined by a property of the tissue and not the probe motion. Although it is not yet clear how this feature might add clinical value, the ability to decouple the material property from the external force, while at the same time preserving signed information in the shear strain field, could well open up interesting avenues for further research.

5 Conclusion

An effective normalization method for axial-shear strain elastography has been proposed. The method produces bounded shear strain data, which facilitates automatic selection of the display range, compensates for variations in the probe motion and preserves the signed values that are important for further analysis. Time averaging the normalized data improves the visualization of shear strain images. In addition, the method is able to decouple certain slip patterns inherent to tissue properties from those induced by the probe motion.

Acknowledgements

We would like to thank Dr. Christopher Uff for providing the *in vivo* data set. This work was funded by Translation Award 081511/Z/06/Z from the Wellcome Trust.

References

[1] J. Ophir, I. Céspedes, H. Ponnekanti, Y. Yazdi, and X. Li, "Elastography: a quantitative method for imaging the elasticity of biological tissues," *Ultrasonic Imaging*, vol. 13, pp. 111–134, 1991.

[2] M. O'Donnell, A. R. Skovoroda, B. M. Shapo, and S. Y. Emelianov, "Internal displacement and strain imaging using ultrasonic speckle tracking," *IEEE Transactions on Ultrasonics, Ferroelectrics, and Frequency Control*, vol. 41, pp. 314–325, 1994.

[3] B. S. Garra, E. I. Céspedes, J. Ophir, S. R. Spratt, R. A. Zuurbier, C. M. Magnant, and M. F. Pennanen, "Elastography of breast lesions: initial clinical results," *Radiology*, vol. 202, pp. 79–86, 1997.

[4] D. M. Regner, G. K. Hesley, N. J. Hangiandreou, M. J. Morton, M. R. Nordland, D. D. Meixner, T. J. Hall, M. A. Farrell, J. N. Mandrekar, W. S. Harmsen, and J. W. Charboneau, "Breast lesions: evaluation with us strain imaging–clinical experience of multiple observers," *Radiology*, vol. 238, no. 2, pp. 425–437, 2006.

[5] E. S. Burnside, T. J. Hall, A. M. Sommer, G. K. Hesley, G. A. Sisney, W. E. Svensson, J. P. Fine, J. Jiang, and N. J. Hangiandreou, "Differentiating benign from malignant solid breast masses with US strain imaging," *Radiology*, vol. 245, no. 2, pp. 401–410, November 2007.

[6] E. Konofagou, T. Harrigan, and J. Ophir, "Shear strain estimation and lesion mobility assessment in elastography," *Ultrasonics*, vol. 38, pp. 400–404, 2000.

[7] A. Thitaikumar, J. Ophir, and T. A. Krouskop, "Noise performance and signal-to-noise ratio of shear strain elastograms," *Ultrasonic imaging*, vol. 27, pp. 145–165, 2005.

[8] A. Thitaikumar, T. A. Krouskop, R. Righetti, and J. Ophir, "Resolution of axial shear strain elastography," *Physics in Medicine and Biology*, vol. 51, pp. 5245–5257, 2006.

[9] A. Thitaikumar, T. A. Krouskop, and J. Ophir, "Signal-to-noise ratio, contrast-to-noise ratio and their trade-offs with resolution in axial-shear strain elastography," *Physics in Medicine and Biology*, vol. 52, pp. 13–28, 2007.

[10] A. Thitaikumar, T. A. Krouskop, B. S. Garra, and J. Ophir, "Visualization of bonding at an inclusion boundary using axial-shear strain elastography: a feasibility study," *Physics in Medicine and Biology*, vol. 52, pp. 2615–2633, 2007.

[11] A. Thitaikumar, L. M. Mobbs, C. M. Kraemer-Chant, B. S. Garra, and J. Ophir, "Breast tumor classification using axial shear strain elastography: a feasibility study," *Physics in Medicine and Biology*, vol. 53, pp. 4809–4823, 2008.

[12] M. Rao, T. Varghese, and E. L. Madsen, "Shear strain imaging using shear deformations," *Medical physics*, vol. 35, no. 2, pp. 412–423, 2008.

[13] H. Chen and T. Varghese, "Principal component analysis of shear strain effects," *Ultrasonics*, vol. 49, pp. 472–483, 2009.

[14] T. Varghese, J. Ophir, and I. Cespedes, "Noise reduction in elastograms using temporal stretching with multicompression averaging," *Ultrasound in Medicine and Biology*, vol. 22, no. 8, pp. 1043–1052, 1996.

[15] J. E. Lindop, G. M. Treece, A. H. Gee, and R. W. Prager, "An intelligent interface for freehand strain imaging," *Ultrasound in Medicine and Biology*, vol. 34, no. 7, pp. 1117–1128, 2008.

[16] L. Chen, R. J. Housden, G. M. Treece, A. H. Gee, and R. W. Prager, "A hybrid displacement estimation method for ultrasonic elasticity imaging," *IEEE Transactions on Ultrasonics, Ferroelectrics, and Frequency Control, in press*, 2010.

[17] P. Chaturvedi, M. F. Insana, and T. J. Hall, "Testing the limitations of 2-D companding for strain imaging using phantoms," *IEEE Transactions on Ultrasonics, Ferroelectrics, and Frequency Control*, vol. 45, pp. 1022–1031, 1998.

[18] J. A. Jensen, "Field: A program for simulating ultrasound systems," in *Proceedings of the 10th Nordic-Baltic Conference on Biomedical Imaging*, Tampere, 1996, pp. 351–353.

[19] M. Bilgen and M. F. Insana, "Elastostatics of a spherical inclusion in homogeneous biological media," *Physics in Medicine and Biology*, vol. 43, pp. 1–20, 1998.

[20] B. Galaz, A. Thitaikumar, and J. Ophir, "Axial-shear strain distributions in an elliptical inclusion model (Part I): a simulation study," in *Proceedings of the Eighth International Conference on the Ultrasonic Measurement and Imaging of Tissue Elasticity*, Vlissingen, Zeeland, The Netherlands, September 2009, p. 99.

[21] A. Thitaikumar, B. Galaz, and J. Ophir, "Axial-shear strain distributions in an elliptical inclusion model (Part II): experimental validation and *in vivo* examples with implications to breast tumor classification," in *Proceedings of the Eighth International Conference on the Ultrasonic Measurement and Imaging of Tissue Elasticity*, Vlissingen, Zeeland, The Netherlands, September 2009, p. 100.